LETTER

Marine heatwaves under global warming

Thomas L. Frölicher[1,2]*, Erich M. Fischer[3] & Nicolas Gruber[4]

Marine heatwaves (MHWs) are periods of extreme warm sea surface temperature that persist for days to months[1] and can extend up to thousands of kilometres[2]. Some of the recently observed marine heatwaves revealed the high vulnerability of marine ecosystems[3–11] and fisheries[12–14] to such extreme climate events. Yet our knowledge about past occurrences[15] and the future progression of MHWs is very limited. Here we use satellite observations and a suite of Earth system model simulations to show that MHWs have already become longer-lasting and more frequent, extensive and intense in the past few decades, and that this trend will accelerate under further global warming. Between 1982 and 2016, we detect a doubling in the number of MHW days, and this number is projected to further increase on average by a factor of 16 for global warming of 1.5 degrees Celsius relative to preindustrial levels and by a factor of 23 for global warming of 2.0 degrees Celsius. However, current national policies for the reduction of global carbon emissions are predicted to result in global warming of about 3.5 degrees Celsius

by the end of the twenty-first century[16], for which models project an average increase in the probability of MHWs by a factor of 41. At this level of warming, MHWs have an average spatial extent that is 21 times bigger than in preindustrial times, last on average 112 days and reach maximum sea surface temperature anomaly intensities of 2.5 degrees Celsius. The largest changes are projected to occur in the western tropical Pacific and Arctic oceans. Today, 87 per cent of MHWs are attributable to human-induced warming, with this ratio increasing to nearly 100 per cent under any global warming scenario exceeding 2 degrees Celsius. Our results suggest that MHWs will become very frequent and extreme under global warming, probably pushing marine organisms and ecosystems to the limits of their resilience and even beyond, which could cause irreversible changes.

There is mounting evidence that global warming is leading to more frequent and intense heatwaves over land, increasing the risk of severe and in some cases irreversible impacts[17]. In comparison, we know much less about how heatwaves in the ocean unfold in time and what
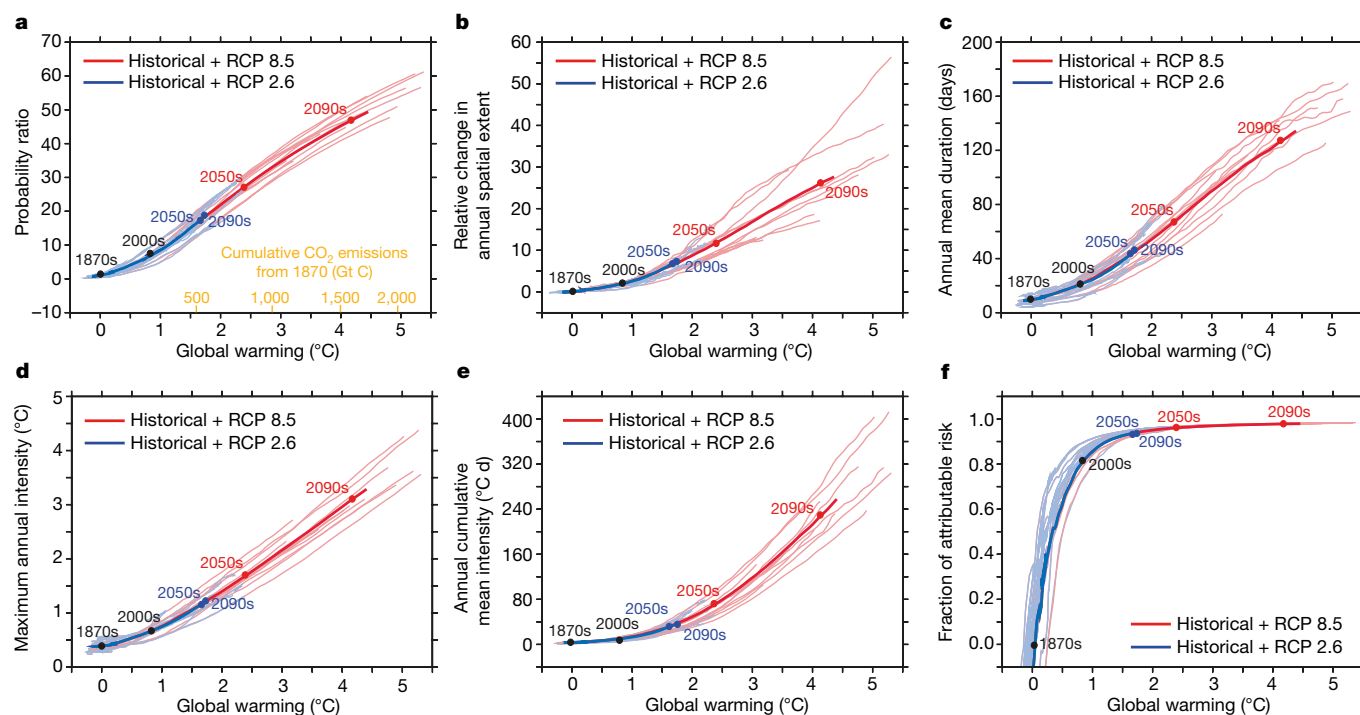

Fig. 1 | Simulated changes in MHW characteristics for different levels of global warming. a, **c**–**f**, Results are shown for the global aggregated annual mean probability ratio (**a**), duration (**c**), maximum intensity (**d**), cumulative mean intensity (**e**) and fraction of attributable risk (**f**) of MHWs exceeding the 99th preindustrial percentile. **b**, Ratio of the mean spatial extent at global warming conditions to that at 1861–1880 conditions. In all panels, the simulated MHW characteristics are plotted against simulated global mean atmospheric surface temperature changes since 1861–1880. The thinner lines represent individual model projections, whereas the thicker lines represent multi-model averages for the RCP 8.5 and RCP 2.6 scenarios. For all models, the historical simulations are merged with the RCP 2.6 and RCP 8.5 simulations. The time series are smoothed with a 20-year running mean and the year labels represent the central year of two decades. The cumulative CO_2 emissions (orange; in gigatons of C) corresponding to different global warming levels are shown in **a**, approximated using the RCP 8.5 ensemble average (see Methods).

[1]Climate and Environmental Physics, Physics Institute, University of Bern, Bern, Switzerland. [2]Oeschger Centre for Climate Change Research, University of Bern, Bern, Switzerland. [3]Institute for Atmospheric and Climate Science, ETH Zürich, Zürich, Switzerland. [4]Environmental Physics, Institute of Biogeochemistry and Pollutant Dynamics, ETH Zürich, Zürich, Switzerland. *e-mail: froelicher@climate.unibe.ch
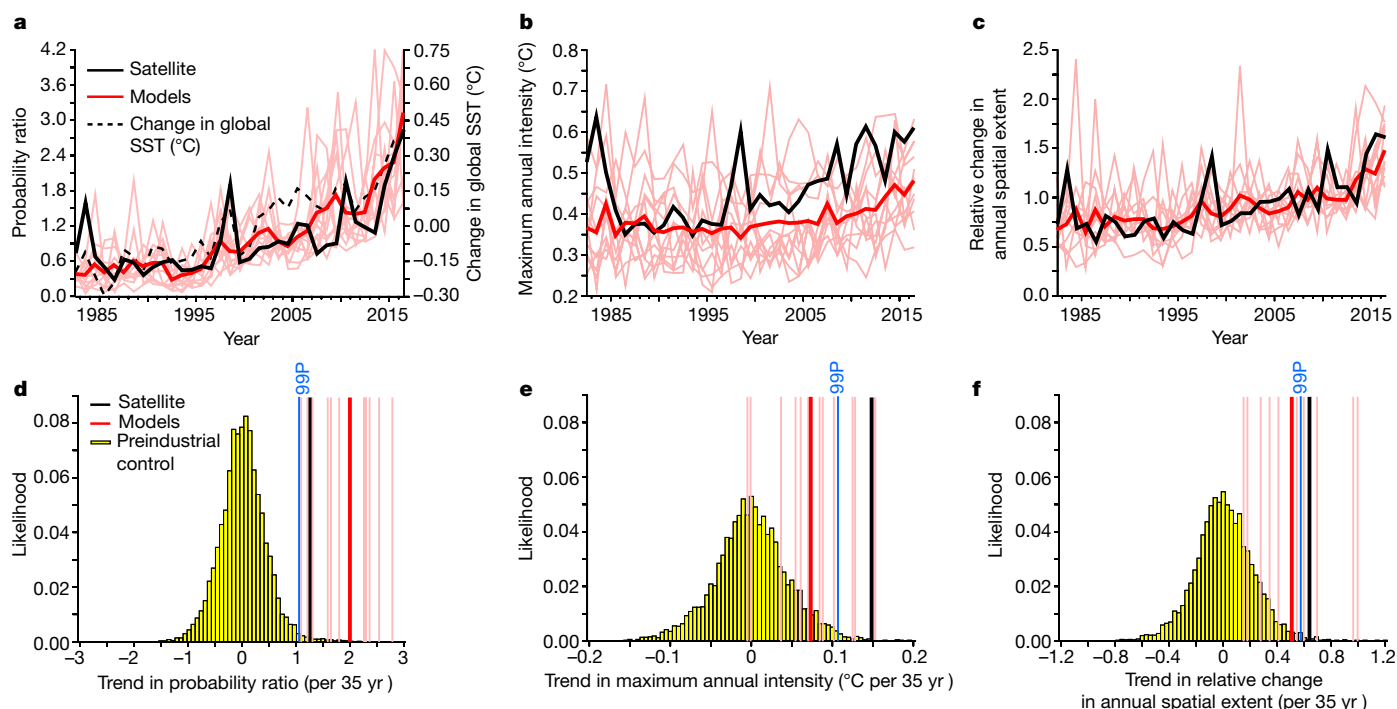
Fig. 2 | Observed and modelled trends in MHW characteristics over the satellite data taking period. a–c, The black lines show the observed changes in the global aggregated probability ratio (**a**), maximum annual intensity (**b**) and the ratio of the annual spatial extent at different years to that at 1982–2016 conditions (**c**) of MHWs exceeding the 1982–2016 99th percentile. The thick red lines indicate the simulated multi-model mean changes and the thin red lines the individual models of MHWs exceeding the 1982–2016 99th percentile. The observed global mean SST changes since 1982–2016 are shown in **a** as a black dashed line. **d–f,** The histograms show simulated 35-year trends of MHW characteristics in the preindustrial control simulations (see Methods for calculation details). The black and red vertical lines show the 35-year observed and simulated trends in 1982–2016 of MHWs exceeding the 1982–2016 99th percentile, and the blue vertical lines show the 99th percentile (labelled as '99P') of the probability density distribution of the preindustrial control simulation trends. The relative changes in the annual spatial extent are calculated as the ratio between the actual mean spatial extent and the average over the 1982–2016 period. Only simulations following the RCP 8.5 scenario are considered here because they best represent observed greenhouse gas emissions since 2006.

the associated impacts are. Although there is a rapidly growing literature on individual events[3,5,8,10,12], the underlying drivers and the degree to which they can be attributed to global warming[10,18] are currently not well known. This knowledge gap is of considerable concern given the high vulnerability of marine ecosystems and fisheries, but also human societies, to such events[19].

One of the first documented impacts of an MHW was the Mediterranean Sea heatwave event in 2003, which led to extensive mortality of benthic marine communities[11]. Other prominent examples are the record-high ocean warming off the coast of Western Australia in early 2011[20], the 2012 MHW in the northwest Atlantic[12], the persistent 2013–2015 extreme warm anomaly of the northeastern Pacific[21] and the 2015/2016 record-warm anomaly across most of the tropical and extratropical oceans[22]. MHWs have caused changes in biological production, toxic algal blooms[7], regime shifts in reef communities[4,8], mass coral bleaching[9] and mortalities of commercially important fish species[13], with cascading impacts on economies and societies[12].

Here, we detect past changes and assess future ones in different MHW characteristics using (i) remotely sensed daily global sea surface temperature (SST) data[22] covering the period 1982–2016, and (ii) daily output from twelve fully coupled global Earth system models (ESMs) covering the period 1861–2100 (see Methods). We identify an event as an MHW when the SST exceeds its local 99th percentile, as determined from daily data from either preindustrial model output or from satellite-based observations and model output over the 1982–2016 period. We then quantify the annual mean probability ratio (the fraction by which the number of MHW days per year has changed), relative change in the annual spatial extent (the average area of an individual heatwave), maximum annual intensity (maximum exceedance of the 99th percentile), annual mean duration (number of days of exceedance) and annual cumulative mean intensity (the product of the duration and the mean

intensity of exceedance). We analyse three distinct periods: the preindustrial period (Fig. 1), the satellite data taking period (1982–2016; Fig. 2) and the future (Figs. 1, 3). We focus on summertime MHWs (that is, hottest days of the year), as many biological processes depend on the absolute temperature. The definition of MHWs needs to be altered, however, when MHWs in colder months can have an impact on biological processes[23].

In preindustrial times, the ESMs suggest that a typical MHW (with reference to preindustrial climatology) lasted 11 days (intermodel range, 6–14 days), had an intensity of up to 0.4 °C (0.3–0.5 °C) and a cumulative mean intensity of 3 °C d (2–4 °C d) (Fig. 1, Extended Data Table 1). MHWs occur coherently with a typical spatial extent of 4.2×10^5 km^2 (1.2×10^5–7.0×10^5 km^2). Under the present-day 1 °C global warming scenario, these models project a nine-fold (6–12) increase in the probability of occurrence of an MHW and a three-fold (1–3) increase in its spatial extent. Further, they project that the duration and the maximum annual and cumulative mean intensity have increased to 25 days (15–33 days), 0.8 °C (0.6–1 °C) and 13 °C d (8–18 °C d), respectively.

These century-scale changes can be put into perspective by determining the trend that they imply over the 35-year period 1982–2016, for which we have satellite observations. To this end, we change the reference for the definition of MHWs to this period. This has virtually no impact on trend computation, but affects the magnitude of the MHW characteristics. Over these 35 years, the models simulate mean changes in the probability ratio and maximum annual intensity of +2.0 (1.1–2.8), +0.07 °C (−0.01 °C to 0.15 °C), respectively, and relative changes in the annual spatial extent of +0.53 (0.17–1.00) (thick red lines in Fig. 2). These multi-model mean trends are at the high end or outside the range of those expected from internal variability (histograms in Fig. 2d–f), which is determined from the preindustrial
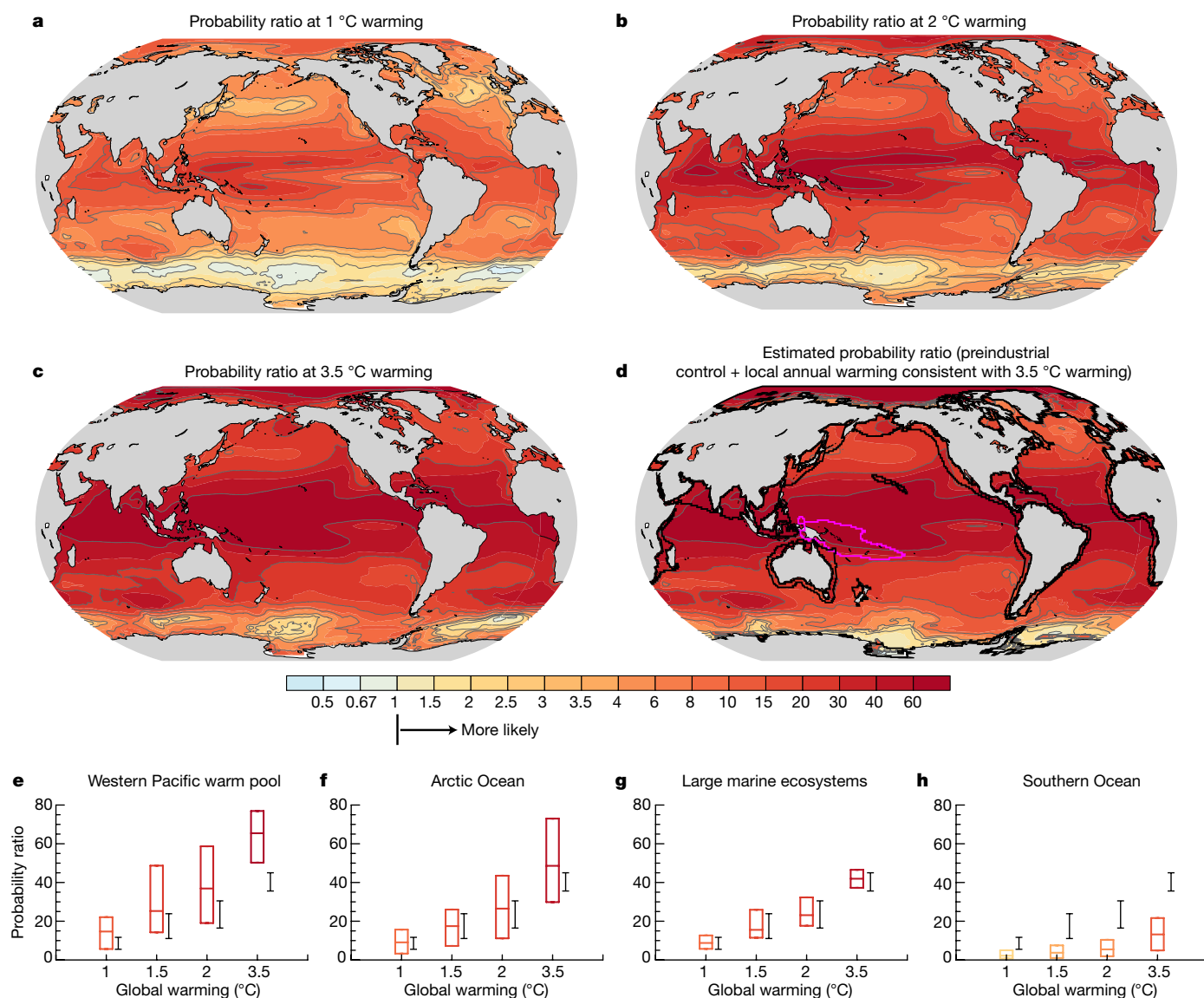
a Probability ratio at 1 °C warming

b Probability ratio at 2 °C warming

c Probability ratio at 3.5 °C warming

d Estimated probability ratio (preindustrial control + local annual warming consistent with 3.5 °C warming)

| 0.5 | 0.67 | 1 | 1.5 | 2 | 2.5 | 3 | 3.5 | 4 | 6 | 8 | 10 | 15 | 20 | 30 | 40 | 60 |

→ More likely

e Western Pacific warm pool

f Arctic Ocean

g Large marine ecosystems

h Southern Ocean

Fig. 3 | Regional changes in probability of MHW days for different global warming levels. a–d, Changes in the probability of MHW days exceeding the preindustrial 99th percentile for a global warming level of 1 °C (**a**), 2 °C (**b**) and 3.5 °C (**c**). To show that the occurrence of MHWs is mainly driven by a simple shift of the whole temperature distribution, in **d** we have added the local annual SST change that is consistent with a 3.5 °C global warming to the preindustrial SST distribution. **e–h**, Changes are regionally aggregated over the western Pacific warm pool (**e**), the Arctic Ocean at >75° N (**f**), large marine ecosystems (**g**) and the Southern Ocean at 45° S–65° S (**h**). Box plots indicate the multi-model mean, minimum and maximum changes in probability, and their colour indicates the value

of the probability ratio, using the same colour coding as for **a–d**. Black bars represent the multi-model minimum and maximum of the global averaged probability changes. In **d**, the western Pacific warm pool region is highlighted by a purple solid contour and the large marine ecosystems are shown with black contours adjacent to the continents in coastal waters. The grey contours in **a–d** highlight pattern structures. The large marine ecosystems provide 95% of the world's annual marine fishery yields[30] and have been developed to enable ecosystem-based marine resource management within ecologically bounded transnational areas. The maps were created using the NCAR Command Language (https://www.ncl.ucar.edu).

control simulations. This indicates that the climate change signal could be strong enough to be detected in observations.

The corresponding 35-year trends in the satellite observations (thick black lines in Fig. 2d–f) are of similar magnitudes as the simulated ones (red lines in Fig. 2d–f). The observations reveal a significant increase in the probability ratio ($+1.29 \pm 0.28$ per 35 years; $P < 0.01$ using a two-sided t-test), maximum intensity ($+0.15 \pm 0.05$ °C per 35 years; $P < 0.01$) and spatial extent ($+0.66 \pm 0.13$ per 35 years; $P < 0.01$) (thick black lines in Fig. 2). These observed trends are statistically significantly outside the model-based estimate of trend variability arising from internal variability, but are within the simulated intermodel uncertainty for trends arising from simulations that include anthropogenic forcing (thin red lines in Fig. 2d–f). Assuming that the model-based estimate of internal variability is accurate, we can conclude with high confidence

that the observed trends in the MHW days, maximum intensity and spatial extent of MHWs are largely caused by long-term ocean warming. Support for this conclusion comes from the fact that SST variations have also a large effect on the year-to-year variability of the different MHW characteristics. The observed temporal evolution of the annual mean SST (black dashed line in Fig. 2a) has strong correlations with the probability ratio ($r^2 = 0.66$ for global SST and probability ratio) and the spatial extent ($r^2 = 0.65$) of MHWs, but relatively weak correlation with their maximal intensity ($r^2 = 0.36$).

The satellite records allow us also to assess the characteristics of the modelled MHWs, allowing us to establish confidence levels for the projections. The modelled spatial pattern in the probability ratio, maximum intensity and the frequency distribution of the spatial extent of MHWs are comparable to the observed ones over the satellite data

taking period (Extended Data Figs. 1, 2), giving us confidence in the corresponding projections. By contrast, the duration, cumulative mean intensity and absolute spatial extent of the MHWs are less well captured by the models, with substantial biases in the corresponding patterns (Extended Data Figs. 1, 2). This indicates that we need to be more careful when interpreting the modelled changes of these characteristics.

For the future and all ocean basins, the ESMs project more frequent, extensive, intense and longer-lasting MHWs (Fig. 1a–e, Fig. 3, Extended Data Tables 1, 2 and Extended Data Fig. 3) (here the reference period is set back to preindustrial times). The magnitude of these changes scales with the global mean temperature and the cumulative CO_2 emissions that drive this global warming (Fig. 1). This scaling is independent of the warming path, that is, it does not depend on whether a particular warming is reached sooner (RCP 8.5, high-emission scenario; see Methods) or later (RCP 2.6, low-emission scenario compatible with the Paris Agreement). It also does not depend on the reference period, as the use of the satellite reference period would only shift this curve slightly to the left (Extended Data Fig. 4a). This allows us to assess the future projections in terms of warming levels rather than the time when this warming is reached.

For 3.5 °C warming, the probability of occurrence of an MHW is 41 times (intermodel range, 36–45 times) higher than in preindustrial times (Fig. 1a, Extended Data Table 2). In other words, a one-in-a-hundred-days event at preindustrial levels is projected to become a one-in-three-days event at this level of global warming. The spatial extent of the annual mean is projected to become 21 (15–29) times larger, its duration to increase to 112 days (92–129 days), and its maximum intensity to rise to 2.5 °C (2.1–2.9 °C) (Fig. 1b–d, Extended Data Table 1). The projected increase in maximum intensity is smaller than the increase in global mean temperature owing to the substantially lower rate of warming by the surface ocean compared to land. The increase in the duration and intensity also leads to a strong increase in the cumulative mean intensity of MHWs of 164 °C d (126–214 °C d) (Fig. 1e, Extended Data Table 1).

These large increases in the different MHW characteristics are substantially reduced if warming is kept below 2 °C, or even below 1.5 °C. The probability of occurrence for an MHW under the 1.5 °C warming scenario is only 40% of that under 3.5 °C warming. The relative change in the spatial extent of a typical MHW would be 25%, the duration 35% and the maximum intensity 45% of those at 3.5 °C.

The probability of MHWs is projected to increase almost everywhere, and the increase is largest in the tropics and the Arctic Ocean and smallest in the Southern Ocean (Fig. 3). The main reason for the large changes in probability in the tropics, and especially in the western Pacific warm pool, is the small variations in SST in these areas, both seasonally and from year to year[24]. As a result, the same changes in annual mean SST lead to much larger changes in the probability of exceeding the 99th percentile. The same applies to the Arctic Ocean, where SST variations below year-round sea ice are very small[25]. This is in contrast to the Southern Ocean, where surface waters are projected to stay relatively cool, and therefore the probability ratio does not increase much under all warming levels. The projected increase in the probability of MHWs in the coastal large marine ecosystems (indicated as black coastal regions in Fig. 3d) has similar magnitude to the global increase under 2 °C warming.

Because of the large increase in the probability ratio with warming, the simulated fraction of attributable risk—that is, the anthropogenic contribution to the probability of an event—reaches 0.87 (0.78–0.91) already under a present-day level of 1 °C warming (Fig. 1f, Extended Data Table 2). This implies (under the assumption that the models simulate naturally occurring MHWs with fidelity) that 87% of the currently occurring MHWs (defined relative to preindustrial conditions) can be attributed to global warming. Because this warming is primarily driven by anthropogenic emissions of greenhouse gases[26], there is a direct link between human action and the simulated increase in MHWs; this supports our conclusion drawn from the satellite data. Clearly, any specific MHW event still arises from the natural variability in the climate

system, but the present-day level of global warming has substantially increased the odds of an MHW to occur. The simulated fraction of attributable risk approaches unity (0.94–0.97) already at 2 °C, implying that essentially all MHWs are due to anthropogenic warming at this or higher levels of warming.

The changes in the occurrence of MHWs are mainly driven by the global-scale shift in mean SSTs. We demonstrate this by adding the simulated spatial warming pattern that is consistent with a global warming of 3.5 °C to the results from the preindustrial control run (Fig. 3d). This yields probability ratio values and patterns that are similar to the results from the transient simulations. It also implies that changing the reference period would not change the relationship between the different MHW characteristics and the amount of warming (Extended Data Fig. 4a). A notable exception is the northern Arctic Ocean, where the SST remains close to freezing temperature during boreal winter months even under the RCP 8.5 scenario[25]. This slightly damps the increase in the probability ratio that would be expected from a global-scale shift in the mean SST.

An important assumption in our analyses is that the employed ESMs simulate MHWs in a sufficiently realistic manner. We consider our results for the probability ratio, maximum intensity and the relative changes in the spatial extent of MHWs to be robust, especially given the good agreement with observations (Fig. 2 and Extended Data Fig. 1) and the relatively small intermodel spread in MHW projections. However, the simulated MHWs last generally longer and are spatially more extensive than observed ones (Extended Data Fig. 1, 2), which is probably caused by the relatively coarse resolution of the ESMs. High-resolution coupled models are needed to resolve mesoscale processes in the atmosphere and the ocean that may be critical to improve the representation of the duration and spatial extent of MHWs. In addition, the conclusion that global warming will lead to a strong increase in all MHW characteristics does not depend on how an MHW is defined (Extended Data Fig. 5), but the quantitative results of MHWs can vary substantially with that definition.

An increase in MHWs will probably increase the risk of severe, pervasive and long-lasting impacts on marine organisms[8], especially on those with reduced mobility and high vulnerability, such as coral reefs, and those living at low latitudes, where many marine species live close to their upper thermal limits[27]. However, the responses of marine organisms and ecosystems to MHWs can be variable and difficult to predict owing to species- and system-specific responses[28,29]. Therefore, better understanding of the response of marine organisms and ecosystems to MHWs and extreme events in other stressors is urgently needed to assess the full risk for marine organisms and ecosystems under global warming.

Online content

Any Methods, including any statements of data availability and Nature Research reporting summaries, along with any additional references and Source Data files, are available in the online version of the paper at https://doi.org/10.1038/s41586-018-0383-9.

1. Hobday, A. J. et al. A hierarchical approach to defining marine heatwaves. *Prog. Oceanogr.* **141**, 227–238 (2016).
2. Scannell, H. A., Pershing, A. J., Alexander, M. A., Thomas, A. C. & Mills, K. E. Frequency of marine heatwaves in the North Atlantic and North Pacific since 1950. *Geophys. Res. Lett.* **43**, 2069–2076 (2016).
3. Marbà, N. & Duarte, C. M. Mediterranean warming triggers seagrass (Posidonia oceanica) shoot mortality. *Glob. Change Biol.* **16**, 2366–2375 (2010).
4. Wernberg, T. et al. An extreme climatic event alters marine ecosystem structure in a global biodiversity hotspot. *Nat. Clim. Change* **3**, 78–82 (2013).
5. Di Lorenzo, E. & Mantua, N. Multi-year persistence of the 2014/15 North Pacific marine heatwave. *Nat. Clim. Change* **6**, 1042–1047 (2016).
6. McCabe, R. M. et al. An unprecedented coastwide toxic algal bloom linked to anomalous ocean conditions. *Geophys. Res. Lett.* **43**, 10,366–10,376 (2016).
7. Cavole, L. et al. Biological impacts of the 2013–2015 warm-water anomaly in the Northeast Pacific: winners, losers, and the future. *Oceanography* **29**, 273–285 (2016).

8. Wernberg, T. et al. Climate-driven regime shift of a temperate marine ecosystem. *Science* **353**, 169–172 (2016).

9. Hughes, T. P. et al. Global warming and recurrent mass bleaching of corals. *Nature* **543**, 373–377 (2017).

10. Oliver, E. C. J. et al. The unprecedented 2015/16 Tasman Sea marine heatwave. *Nat. Commun.* **8**, 16101 (2017).

11. Garrabou, J. et al. Mass mortality in Northwestern Mediterranean rocky benthic communities: effects of the 2003 heat wave. *Glob. Change Biol.* **15**, 1090–1103 (2009).

12. Mills, K. E. et al. Fisheries management in a changing climate: lessons form the 2012 ocean heat wave in the Northwest Atlantic. *Oceanography* **26**, 191–195 (2014).

13. Caputi, N. et al. Management adaptation of invertebrate fisheries to an extreme marine heat wave event at a global warming hot spot. *Ecol. Evol.* **6**, 3583–3593 (2016).

14. Pershing, A. J. et al. Slow adaptation in the face of rapid warming leads to collapse of the Gulf of Maine cod fishery. *Science* **350**, 809–812 (2015).

15. Oliver, E. C. J. et al. Longer and more frequent marine heatwaves over the past century. *Nat. Commun.* **9**, 1324 (2018).

16. Climate Action Tracker. *Improvement in warming outlook as India and China move ahead, but Paris Agreement gap still looms large* (2017); https://climateactiontracker.org/documents/61/CAT_2017-11-15_ ImprovementInWarmingOutlook_BriefingPaper.pdf.

17. Pachauri, R. K. & Meyer, L. A. (eds.) *Climate Change 2014: Synthesis Report. Contribution of Working Groups I, II and III to the Fifth Assessment Report of the Intergovernmental Panel on Climate Change* (IPCC, Geneva, 2014).

18. Walsh, J. E. et al. The high latitude marine heat wave of 2016 and its impacts on Alaska. *Bull. Am. Meteorol. Soc.* **99**, 39–43 (2018).

19. Frölicher, T. L. & Laufkötter, C. Emerging risks from marine heat waves. *Nat. Commun.* **9**, 650 (2018).

20. Pearce, A. F. & Feng, M. The rise and fall of the 'marine heat wave' off Western Australia during the summer of 2010/2011. *J. Mar. Syst.* **111–112**, 139–156 (2013).

21. Bond, N. A., Cronin, M. F., Freeland, H. & Mantua, N. Causes and impacts of the 2014 warm anomaly in the NE Pacific. *Geophys. Res. Lett.* **42**, 3414–3420 (2015).

22. Banzon, V., Smith, T. M., Liu, C. & Hankins, W. A long-term record of blended satellite and in situ sea surface temperature for climate monitoring, modeling and environmental studies. *Earth Syst. Sci. Data* **8**, 165–176 (2016).

23. Morley, J. W., Batt, R. D. & Pinsky, M. L. Marine assemblages respond rapidly to winter climate variability. *Glob. Change Biol.* **23**, 2590–2601 (2017).

24. Frölicher, T. L., Rodgers, K. B., Stock, C. A. & Cheung, W. W. L. Sources of uncertainties in 21st century projections of potential ocean ecosystem stressors. *Glob. Biogeochem. Cycles* **30**, 1224–1243 (2016).

25. Carton, J. A., Ding, Y. & Arrigo, K. R. The seasonal cycle of the Arctic Ocean under climate change. *Geophys. Res. Lett.* **42**, 7681–7686 (2015).

26. Bindoff, N. L. et al. *Detection and Attribution of Climate Change: from Global to Regional. Climate Change 2013: The Physical Science Basis. Contribution of Working Group I to the Fifth Assessment Report of the Intergovernmental Panel on Climate Change* (Cambridge Univ. Press, Cambridge, 2013).

27. Comte, L. & Olden, J. D. Climatic vulnerability of the world's freshwater and marine fishes. *Nat. Clim. Change* **7**, 718–722 (2017).

28. Logan, C. A., Dunne, J. P., Eakin, C. M. & Donner, S. D. Incorporating adaptive responses into future projections of coral bleaching. *Glob. Change Biol.* **20**, 125–139 (2014).

29. Donelson, J. M., Munday, P. L., McCormick, M. I. & Pitcher, C. R. Rapid transgenerational acclimation of a tropical reef fish to climate change. *Nat. Clim. Change* **2**, 30–32 (2012).

30. Stock, C. A. et al. Reconciling fisheries catch and ocean productivity. *Proc. Natl Acad. Sci. USA* **114**, E1441–E1449 (2017).

Reviewer information *Nature* thanks R. Asch, E. Oliver and the other anonymous reviewer(s) for their contribution to the peer review of this work.

Author contributions All authors designed the study. T.L.F. performed the analysis and wrote the manuscript together with N.G., with substantial input from E.M.F.

Competing interests The authors declare no competing interests.

Additional information
Extended data is available for this paper at https://doi.org/10.1038/s41586-018-0383-9.
Reprints and permissions information is available at http://www.nature.com/reprints.
Correspondence and requests for materials should be addressed to T.L.F.
Publisher's note: Springer Nature remains neutral with regard to jurisdictional claims in published maps and institutional affiliations.

METHODS

We analyse daily SST and surface atmospheric temperature data from simulations (using the first ensemble member, r1i1p1) of twelve coupled ESMs that were considered in the fifth phase of the Coupled Model Intercomparison Project (CMIP5) and for which the output necessary to analyse changes in daily SST was available (Extended Data Table 3). All model simulations were run over the historical 1861–2005 period and over the 2006–2100 period, following both a high-emission scenario (RCP 8.5; RCP, representative concentration pathway) and a low-emission scenario compatible with the Paris Agreement (RCP 2.6).

In addition, we use the National Oceanic and Atmospheric Administration's ¼° daily optimum interpolation SST dataset[22,31] version 2.0, obtained by the Advanced Very High Resolution Radiometer and covering the period 1 January 1982 to 31 December 2016 (www.ncdc.noaa.gov/oisst/; accessed on 6 July 2017). The dataset combines observations from different platforms, such as satellites, ships and buoys, and includes bias adjustment of satellite and ship observations to compensate for platform differences and sensor biases. For comparison with the coarse-resolution models, the $0.25° \times 0.25°$ satellite data were regridded daily onto a regular $1° \times 1°$ grid by averaging over the 1°-grid cells before calculating the characteristics of the MHW.

We define an event as an MHW when the daily SST exceeds the 99th percentile (a one-in-a-hundred-days event). We test the sensitivity of the results by also using the 90th (a one-in-ten-days event), the 99.9th (a one-in-2.74-years event) and the 99.99th (a one-in-27.4-years event) percentiles (Extended Data Fig. 5). The percentiles are calculated for each grid cell from multi-centennial preindustrial control simulations (most simulations are for 500 years or longer). This ensures that even the local 99.99th percentile is well defined. The same preindustrial control simulation is used to define the reference global mean temperature relative to which the warming targets are computed. Changing the reference period to present-day (that is, 2007–2026; ±10 years centred around today) would just shift the values on the x axis in all panels of Fig. 1, but would not change the relationship between the different MHW characteristics and the amount of global warming (Extended Data Fig. 4a). Because some models have constant year-round SSTs in a few grid cells under sea ice in the preindustrial control simulations, grid cells in which the average yearly number of MHWs over the entire control simulation deviates by more than 5% from the theoretical number (for example, 3.65 days for the 99th percentile) are masked out. For the analysis of atmospheric heatwaves over land, we use the same definition as for MHWs. For analysis over the satellite data taking period, we use the entire 1982–2016 period as the baseline period for both the models and the satellite data.

The usage of a percentile-based threshold allows the quantification of MHWs across locations that differ in variability. An absolute threshold would only be relevant in terms of impacts in some regions but not in others. By using percentile-based characteristics, no assumption is made regarding the underlying probability temperature distribution, and potential model-observation biases in the mean and higher-order statistical moments of the probability temperature distribution are implicitly taken into account. This increases our confidence in the simulated probability ratio, but the simulated spatial extent and duration (and intensity) of MHWs may still differ from observations. Our definition differs from that proposed by Hobday et al.[2], who define an MHW by using a much lower seasonally varying percentile threshold (90th rather than 99th), but impose a duration of at least five days. Relative to the results obtained with our definition, the definition of Hobday et al. would lead to an increase of the number of heat-wave days, including the cold seasons, because the vast majority of our heatwaves last longer than five days. However, using their definition would not change our conclusion about the robust increase in all MHW metrics under global warming, because this result is essentially insensitive to the percentile threshold that we choose (Extended Data Fig. 5).

For each MHW, we calculate a series of characteristics, such as the duration (in days; number of days of percentile threshold exceedance), the maximum intensity (in °C; maximum SST anomaly with respect to the percentile threshold over the duration of the heatwave), the spatial extent (in km²), the cumulative mean intensity (in °C d; the mean intensity multiplied with the duration of an event), and the probability ratio, $PR = P_1/P_0$, where P_1 is the probability of exceeding a relative threshold at any given point in time (for example, today) and P_0 the probability of exceeding that threshold during the preindustrial control or satellite climatological period. The cumulative mean intensity may indicate the integrated impact of an MHW on an organism's health—a similar measure, the degree heating days or weeks, is commonly used to identify areas where substantial coral bleaching is likely to occur[32]. We then calculate annual statistics, including the number of MHW days per year, the changes in the annual averaged spatial extent of an MHW relative to 1861–1880 or the satellite climatological period, the annual mean duration of single contiguous MHW events in a given year, the maximum annual intensity, the annual mean cumulative mean intensity and the annual mean fraction of attributable risk ($FAR = 1 - P_0/P_1$)[10,18,33–36].

Because the observed global warming primarily results from human influence, we can attribute the changes in the occurrence of MHWs to human-induced global warming[33]. The FAR was initially introduced to represent a fraction of the probability of individual observed events[33,37]. Here, we extend the FAR framework to the global scale[34,38,39] to represent the probability for a class of events exceeding a certain threshold over the globe. For a given MHW, the probability ratio can be interpreted as a change in the odds of the occurrence of local SST anomalies exceeding a certain local threshold. The regional or global aggregated probability ratio expresses a change in the global occurrence of SST anomalies exceeding local thresholds.

We calculate the MHW properties by using slightly different frameworks. The probability ratio, maximum intensity, duration, cumulative mean intensity and FAR are defined when local (grid-cell) SST exceeds the local 99th percentile and where adjacent grid cells can have different values. The intensity and duration refers to the properties of a contiguous event, but the probability ratio refers to MHW days per year, regardless of how they are distributed across different events. For the spatial extent, we aggregate adjacent grid cells that are above the 99th percentile together to form a single event. To calculate the spatial extent of individual MHWs, we isolate the individual MHWs per day using the function *skimage.measure.label* of the Python image processing tool scikit-image. The global estimate of these characteristics is calculated with an area-weighted average across all ocean grid points in each year from 1861 to 2100. All MHW characteristics are calculated on the native model grid, which differs in resolution across the models, but multi-model means and globally aggregated characteristics are calculated and shown on a regular $1° \times 1°$ grid.

We usually express the changes in MHW characteristics as changes for particular global warming levels (that is, 1 °C, 2 °C and 3.5 °C). These global warming levels are calculated for each model and scenario individually by subtracting the simulated global annual mean atmospheric surface temperature, averaged over the 20-year period centred around the year when the respective global warming level is reached, from the simulated global mean atmospheric surface temperature averaged over the 1861–1880 period.

The cumulative CO_2 emissions corresponding to the different global warming levels (orange ticks on horizontal axis in Fig. 1a) are approximated using calculated cumulative CO_2 emissions from the RCP 8.5 average of eight models for which necessary data were available (Extended Data Table 3). This means that 500 Gt C corresponds to 1.6 °C, 1,000 Gt C to 2.8 °C, 1,500 Gt C to 4.0 °C and 2,000 Gt C to 4.9 °C. No uncertainties are assigned to these values. We note that these eight models as a class have a relatively low transient climate response to cumulative carbon emissions, and therefore cumulative carbon emission estimates for a certain global warming level are relatively large[40].

To test whether the observed multi-decadal trends over the satellite data taking period are different from what would be expected from internal variability, we compare the observed global aggregated trends in the probability ratio, maximum intensity and spatial extent with the probability density function of 35-year-long trends derived from the 12 multi-century control simulations of the different ESMs. In total, we calculated 6,460 35-year trends.

We also used a ten-member ensemble simulation of the NCAR-DOE CESM model[34] to show that internal variability may induce uncertainty at the local level, but plays a negligible role in explaining the global changes in the different MHW characteristics, as all ten realizations yield very similar results (Extended Data Fig. 4). We also show that our simulated changes in the MHW characteristics do not depend on the choice of calculation method for the climatological 99th percentiles. In fact, the simulated changes in the MHW characteristics are similar when determining the local 99th percentiles from a simulation of the GFDL ESM2M model forced with observed solar and volcanic boundary conditions but with greenhouse gases and aerosols concentration set to preindustrial levels (Extended Data Fig. 6). Only the NCAR-DOE CESM and GFDL ESM2M models provide the daily output necessary to analyse the sensitivity of the results to internal variability and to the calculation of the climatological baseline period.

We used the western equatorial Pacific biome definition of Fay and McKinley[41] to highlight the western Pacific warm pool region in Fig. 3. The biogeographical biomes in ref. [41] are defined by distinct SSTs, maximum mixed-layer depths and summer chlorophyll concentrations, and capture patterns of large-scale biogeochemical function at the basin scales.

Under any level of warming, MHWs are projected to occur much more frequently than land-based heatwaves (Extended Data Table 2). The probability of MHW days is about 1.6 times higher than that for land-based heatwave days under 2 °C global warming, even though the global SSTs are projected to increase by only 0.55 °C per degree of surface air temperature warming over land (Extended Data Fig. 7). The larger increase in the probability ratio is obtained because the temperature variability over land is much larger than over the ocean[19], leading to a smaller signal-to-noise ratio. This is evidenced by the 8.0 °C difference between the 99th percentile and the annual mean air temperature averaged over the global

land surface at preindustrial times, which is much larger than the 3.7 °C difference over the ocean.

In general, the probability ratio, and therefore also the FAR, increase the most for very rare extremes (Extended Data Table 2); that is, they increase much more if MHWs are defined with more extreme preindustrial percentile thresholds (Extended Data Fig. 5). For example, the probability ratio is 9 (intermodal range, 6–12) for moderate MHWs (defined with the 99th preindustrial percentile) and 141 (47–296) for the rarest MHWs (99.99th preindustrial percentile) under 1 °C global warming.

Code availability. The code used to produce the figures in this paper is available from the corresponding author upon request.

Data availability. The CMIP5 data used for this study can be accessed at http://pcmdi9.llnl.gov/ and the satellite SST observations can be accessed at www.ncdc.noaa.gov/oisst/. Other datasets generated during the current study are available from the corresponding author upon reasonable request.

31. Reynolds, R. W. et al. Daily high-resolution-blended analyses for sea surface temperature. *J. Clim.* **20**, 5473–5496 (2007).
32. Eakin, C. M. et al. Caribbean corals in crisis: record thermal stress, bleaching, and mortality in 2005. *PLoS One* **5**, e13969 (2010).
33. Stott, P., Stone, D. & Allen, M. Human contribution to the European heatwave of 2003. *Nature* **432**, 610–614 (2004); corrigendum **436**, 1200 (2005).
34. Fischer, E. M. & Knutti, R. Anthropogenic contribution to global occurrence of heavy-precipitation and high-temperature extremes. *Nat. Clim. Change* **5**, 560–564 (2015).
35. Jacox, M. G., Alexander, M. A., Mantua, N. & Scott, J. D. Forcing of multiyear extreme ocean temperatures that impacted California Current marine resources in 2016. *Bull. Am. Meteorol. Soc.* **99**, 27–33 (2018).
36. Newman, M., Wittenberg, A. T., Cheng, L., Compo, G. P. & Smith, C. A. The extreme 2015/16 El Nino, in the context of historical climate variability and change. *Bull. Am. Meteorol. Soc.* **99**, 16–20 (2018).
37. Allen, M. R. & Ingram, W. J. Constraints on future changes in climate and the hydrologic cycle. *Nature* **419**, 224–232 (2002); corrigendum **489**, 590 (2012).
38. Angélil, O. et al. Attribution of extreme weather to anthropogenic greenhouse gas emissions: Sensitivity to spatial and temporal scales. *Geophys. Res. Lett.* **41**, 2150–2155 (2014).
39. King, A. D. et al. Emergence of heat extremes attributable to anthropogenic influences. *Geophys. Res. Lett.* **43**, 3438–3443 (2016).
40. Frölicher, T. L. & Paynter, D. J. Extending the relationship between global warming and cumulative carbon emissions to multi-millennial timescales. *Environ. Res. Lett.* **10**, 075002 (2015).
41. Fay, A. R. & McKinley, G. A. Global ocean biomes: mean and temporal variability. *Earth Syst. Sci. Data* **7**, 107–128 (2014).
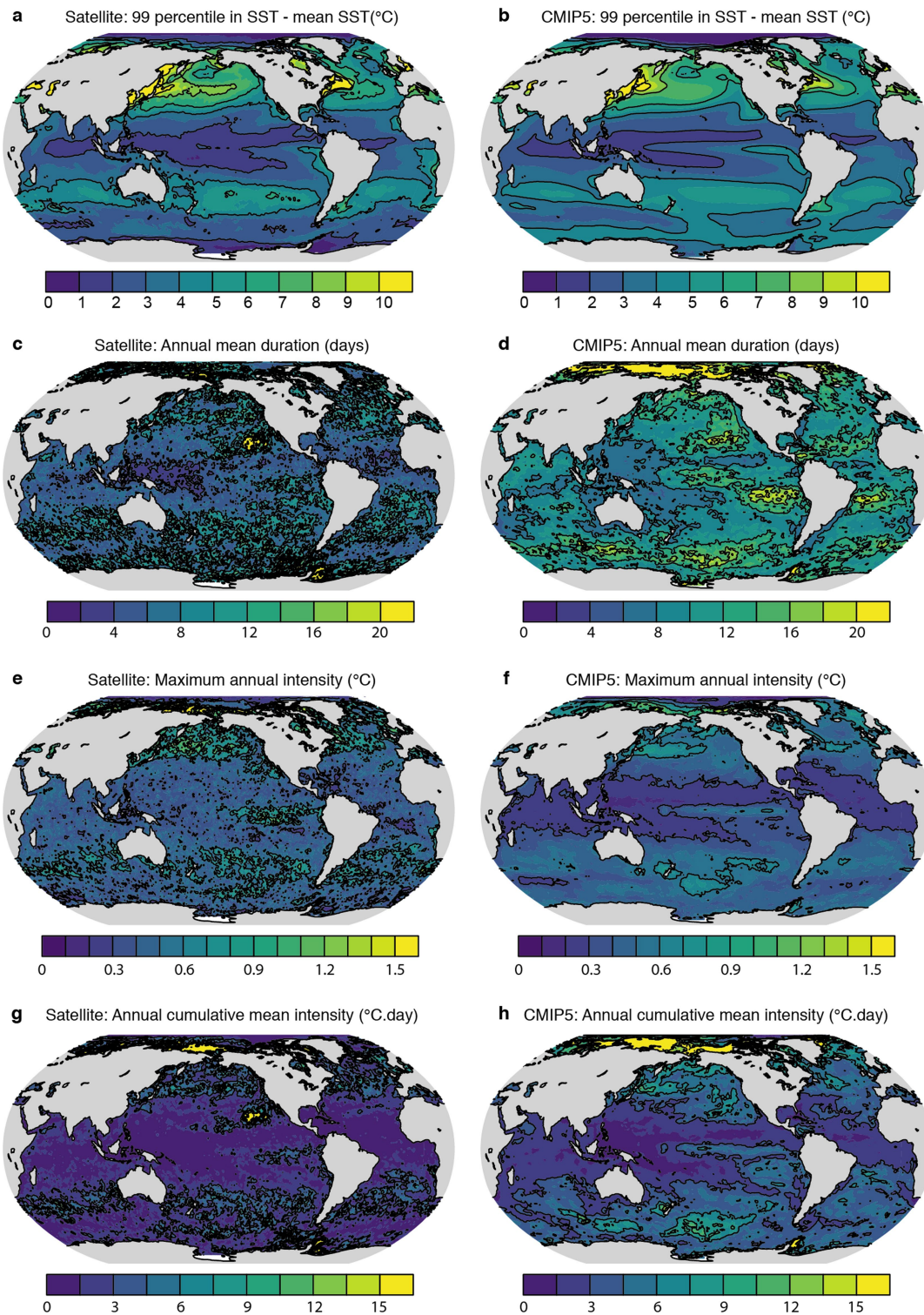
Extended Data Fig. 1 | Observed and simulated MHW characteristics exceeding the 1982–2016 99th percentile, averaged over the 1982–2016 period. a, b, Differences between the 99th percentile in SST and the annual mean SST. **c, d,** Annual mean duration of MHWs. **e, f,** Maximum annual intensity of MHWs. **g, h,** Annual cumulative mean intensity of MHWs. Satellite-derived patterns (**a, c, e, g**) and CMIP5 multi-model mean patterns (**b, d, f, h**). The black contours in all panels highlight the pattern structures. The spatial correlation between the CMIP5 multi-model mean and the satellite-based estimates is $r^2 = 0.80$ for **a** and **b**, $r^2 = 0.15$ for **c** and **d**, $r^2 = 0.43$ for **e** and **f**, and $r^2 = 0.18$ for **g** and **h**.

a

b

c
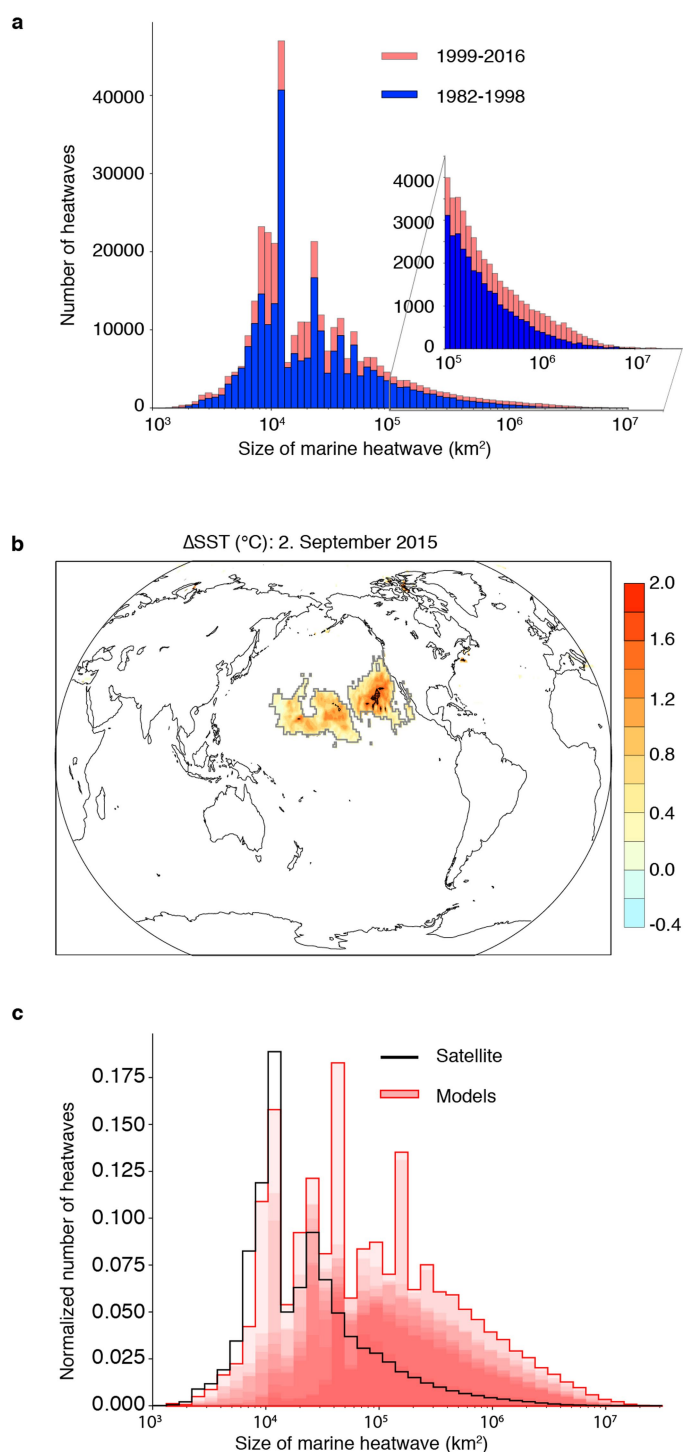
Extended Data Fig. 2 | Spatial extent of observed and simulated MHWs over the satellite data taking period. a, Histogram of the spatial extent of satellite-observed MHWs above the climatological (1982–2016) 99th percentile for the 1982–1998 (blue) and 1999–2016 (red) period. **b**, The spatial pattern of the MHW with the largest extent in the satellite data taking period (1982–2016), which occurred on 2 September 2015 in the North Pacific and was associated with the 'the Blob'[21]. It had a spatial extent of about twice the area of the United States (that is, $1.85 \times 10^7 \, km^2$). Shown are SST anomalies above the 1982–2016 climatological 99th percentile on 2 September 2015. The colour bar shows degrees Celsius. **c**, Comparison between satellite-based observations (black line) and simulations (red histogram) of the spatial extent of MHWs above the climatological 99th percentile over the 1982–2016 period. The number of MHWs (y axis) is normalized with the total number of MHWs. Deeper red colour indicates a greater number of overlapping models.
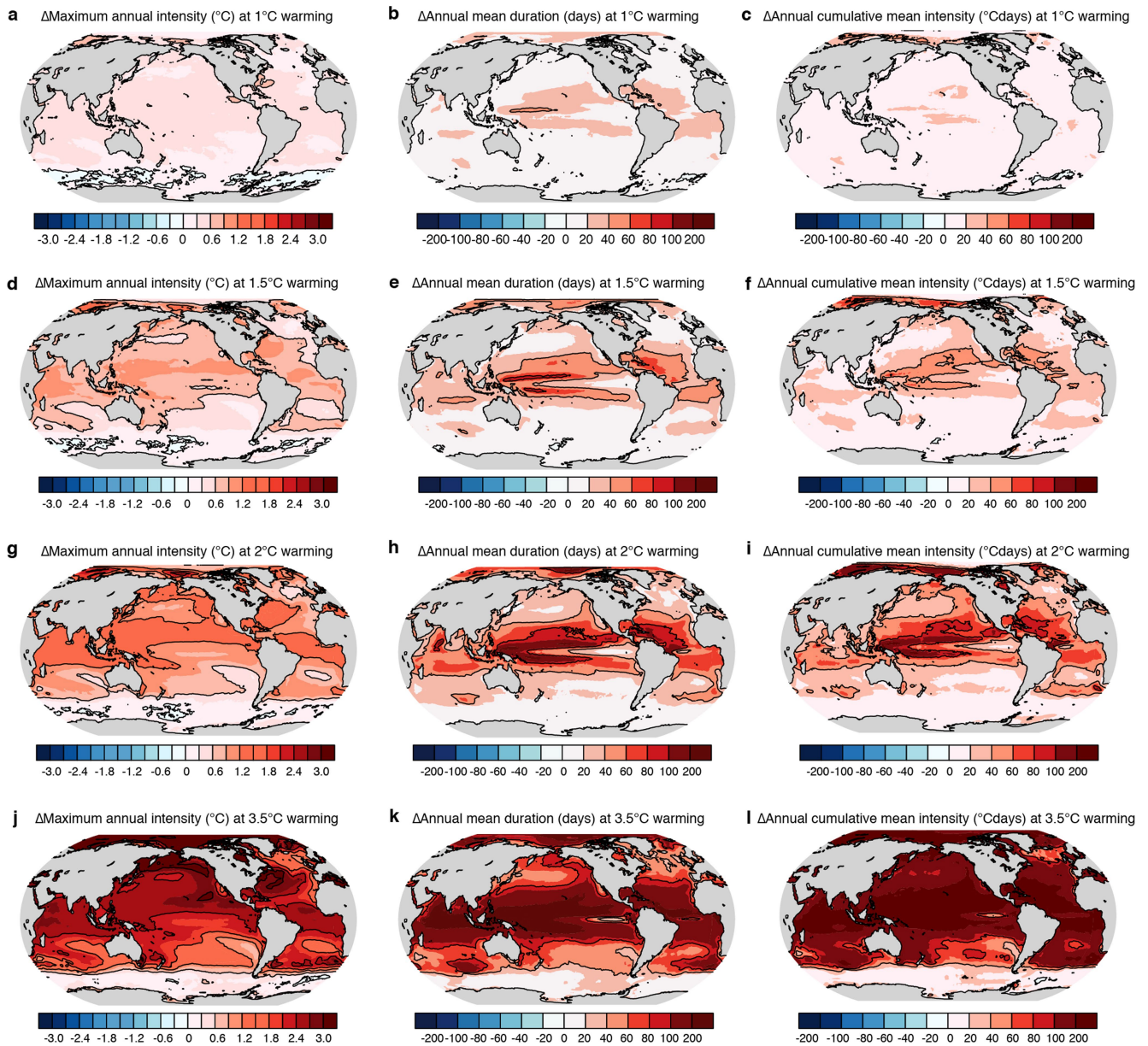
Extended Data Fig. 3 | Simulated multi-model mean changes in different MHW characteristics exceeding the preindustrial 99th percentile since preindustrial times for different global warming levels. a–l, Changes in the maximum annual intensity (**a**, **d**, **g**, **j**), annual mean duration (**b**, **e**, **h**, **k**) and annual cumulative mean intensity (**c**, **f**, **i**, **l**) of MHWs for global warming of 1 °C (**a**–**c**), 1.5 °C (**d**–**f**), 2 °C (**g**–**i**) and 3.5 °C (**j**–**l**). The black contours highlight the pattern of changes.
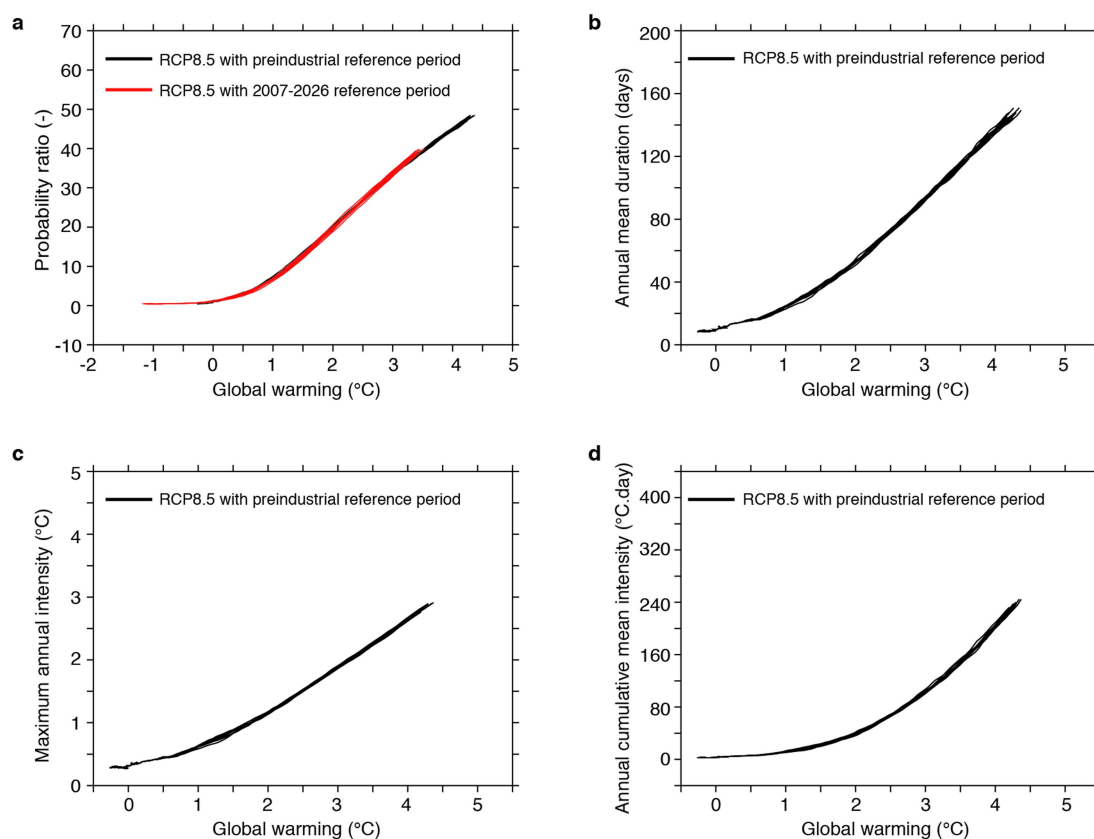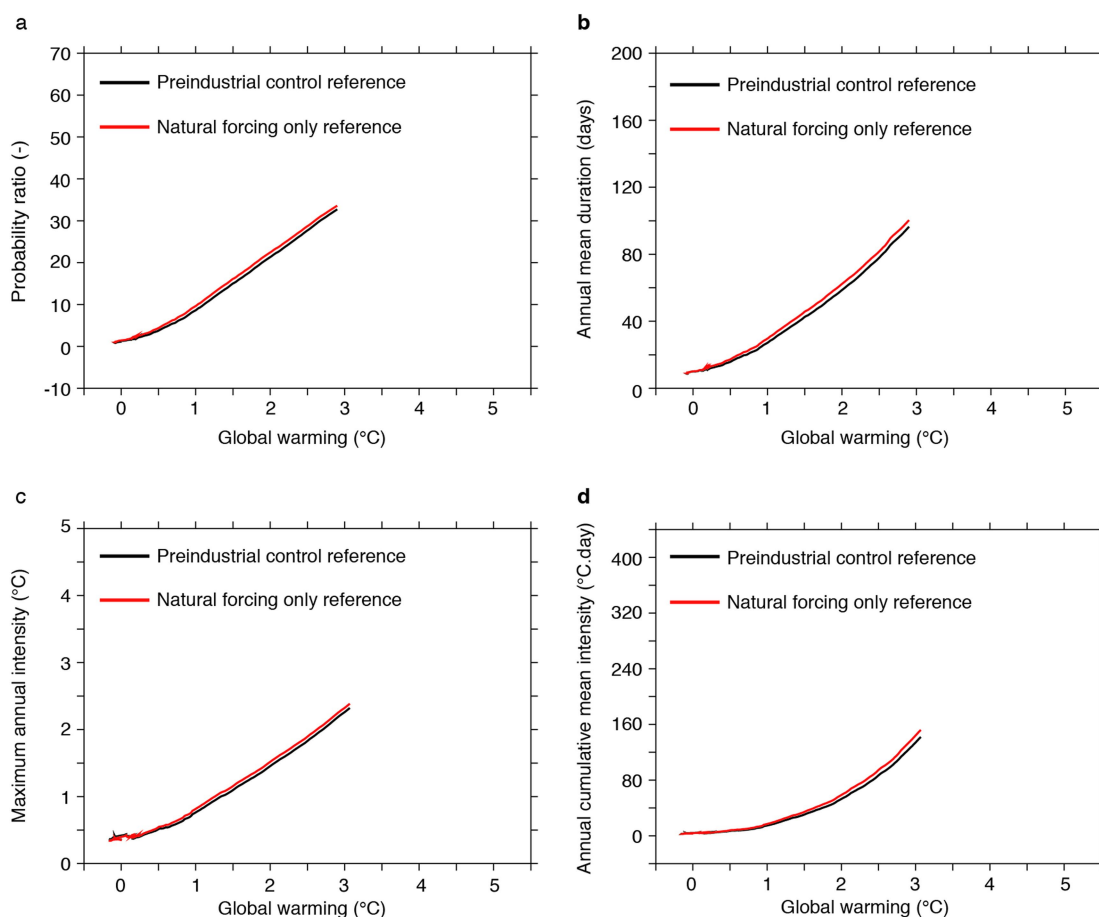
Extended Data Fig. 4 | Simulated changes in different MHW characteristics exceeding the preindustrial 99th percentile. The data were obtained from a 10-member ensemble simulation with NCAR-DOE CESM[34]. **a**–**d**, The probability ratio (**a**), annual mean duration (**b**), maximum annual intensity (**c**) and annual cumulative mean intensity (**d**) of MHWs. The black lines show the individual ensemble members. The red line in **a** shows the probability ratio versus global warming for a reference period that is defined as the 99th percentile over the 2007–2026 period, obtained using all ten ensemble members. The ensemble members are initialized from different starting points (ocean, sea ice, land and atmosphere) in the preindustrial control simulation. The simulations follow the RCP 8.5 scenario over the 21st century. The time series are smoothed with a 20-year running mean.
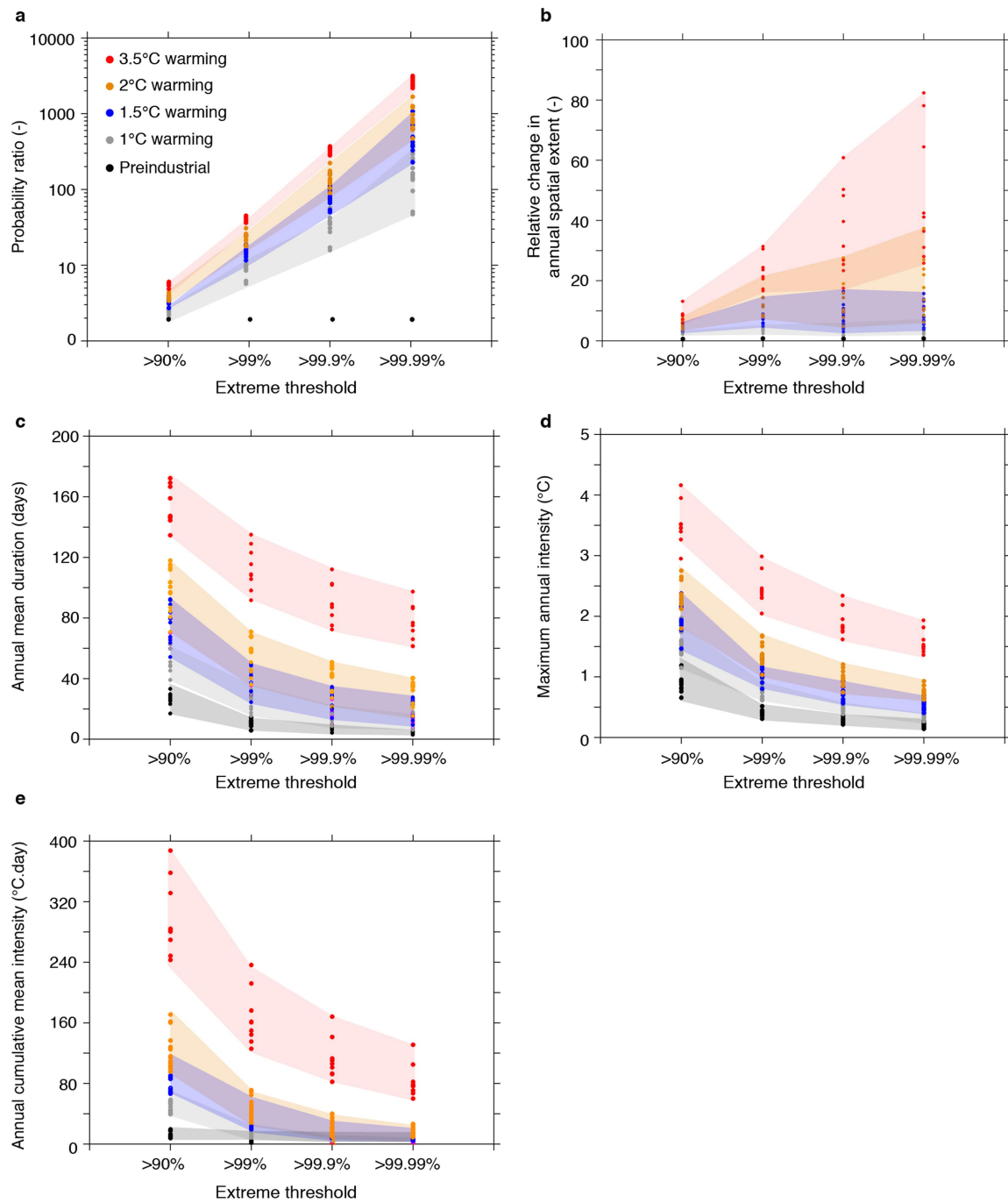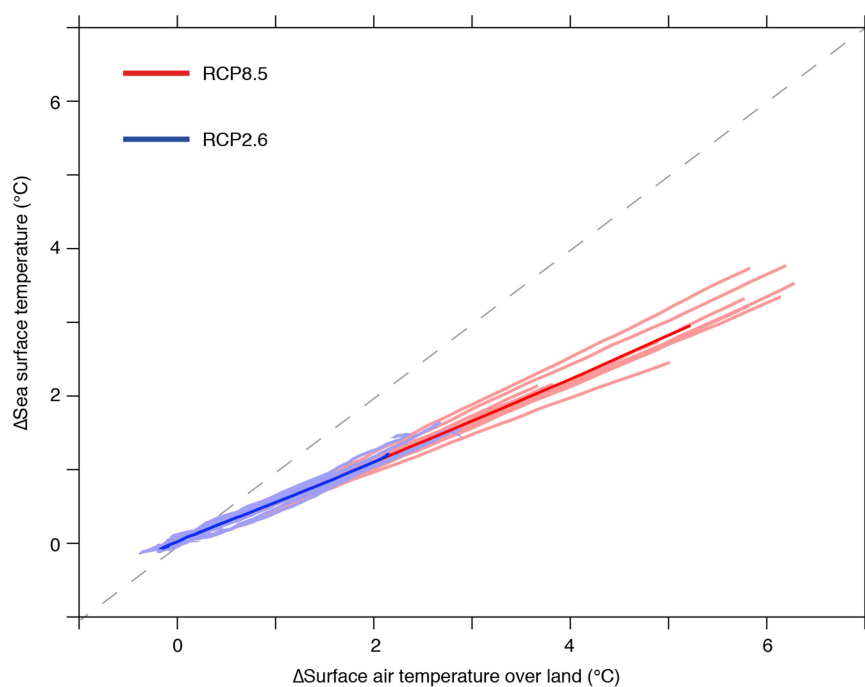
Extended Data Fig. 5 | Simulated changes in MHW characteristics for different global warming levels and different extreme thresholds. a, c–e, Global annual mean probability ratio (a; logarithmic scale), duration (c), maximum intensity (d) and cumulative mean intensity (e) of MHWs versus different extreme thresholds for different changes in global mean surface air temperature. b, Changes in the ratio of the mean spatial extent of MHWs between global warming conditions and 1861–1880 conditions. Simulations following only the RCP 8.5 scenario are shown. The shaded areas indicate the maximum range simulated by the CMIP5 models.

Extended Data Fig. 6 | Comparison between simulated changes in MHW characteristics exceeding the 99th percentile from a natural-forcing simulation and from a preindustrial control simulation using GFDL ESM2M forced with the RCP 8.5 scenario over the 21st century. a–d, The probability ratio (**a**), annual mean duration (**b**), maximum annual intensity (**c**) and annual cumulative mean intensity (**d**) of MHWs.

The red line shows the simulated changes exceeding the 99th percentile from a natural-forcing simulation of GFDL ESM2M forced with observed solar and volcanic boundary conditions, but with greenhouse gases and aerosol concentrations set to preindustrial. The black line shows the simulated changes exceeding the preindustrial 99th percentile. The time series are smoothed with a 20-year running mean.

Extended Data Fig. 7 | Simulated changes in global SST as a function of global surface air temperature over land. The light red and blue lines represent individual model projections, whereas the dark red and blue lines represent multi-model averages for the RCP 8.5 (red) and RCP 2.6 (blue) scenarios. The time series are smoothed with a 20-year running mean. The grey dashed 1:1 line is shown for reference.

Extended Data Table 1 | Simulated changes in the annual mean spatial extent of MHWs relative to preindustrial times, and simulated annual mean duration, maximum and cumulative mean intensity of MHWs exceeding the preindustrial 99th percentile for different global warming levels

Warming	Relative change in annual mean spatial extent (-)	Annual mean duration (days)	Maximum annual intensity (°C)	Annual cumulative mean intensity (°C days)
Preindustrial	-	11 (6/14)	0.41 (0.31/0.52)	3 (2/4)
1°C	2.6 (3.4/1.3)	25 (15/33)	0.78 (0.62/1.01)	13 (8/18)
1.5°C	5.6 (11.5/3.0)	39 (24/49)	1.11 (0.83/1.40)	28 (19/42)
2°C	9.1 (18.0/6.0)	55 (36/71)	1.45 (1.09/1.79)	49 (30/71)
3.5°C	20.7 (29.1/14.9)	112 (92/129)	2.53 (2.12/2.93)	164 (126/214)

Multi-model mean estimates are shown and the associated minimum and maximum model estimates are given in parentheses.

Extended Data Table 2 | Simulated probability ratio and fraction of attributable risk estimates averaged over the ocean and over land for different global warming levels and for different preindustrial percentile thresholds (99th and 99.99th)

	99th percentile		99.99th percentile
Probability ratio			
Warming	Ocean	Land	Ocean
1°C	8.94 (5.70/12.15)	5.56 (3.44/8.75)	141 (47/296)
1.5°C	15.65 (11.34/24.48)	9.71 (6.63/13.48)	418 (197/1079)
2°C	22.80 (16.31/30.76)	13.89 (10.71/18.59)	893 (448/1679)
3.5°C	41.19 (36.32/44.91)	26.50 (22.36/30.26)	2560 (2094/2913)
Fraction of attributable risk			
Warming	Ocean	Land	Ocean
1°C	0.87 (0.78/0.91)	0.78 (0.65/0.87)	0.98 (0.94/0.99)
1.5°C	0.93 (0.90/0.96)	0.88 (0.83/0.92)	1 (0.99/1)
2°C	0.95 (0.94/0.97)	0.92 (0.90/0.95)	1
3.5°C	0.97 (0.97/0.98)	0.96 (0.95/0.96)	1

Values are multi-model means, and minimum and maximum model estimates are shown in parentheses.

Extended Data Table 3 | Global climate models used in this study

Model
CanESM2 (800)*
CSIRO-Mk3-6-0 (500)
GFDL-CM3 (500)
GFDL-ESM2G (500)*
GFDL-ESM2M (500)*
HadGEM2-ES (500)*
IPSL-CM5A-LR (1000)*
IPSL-CM5A-MR (300)*
MIROC-ESM (630)*
MPI-ESM-LR (1000)*
MPI-ESM-MR (150)
MRI-CGCM3 (500)

The numbers indicate the length of the control simulation analysed.
*Models used to calculate the diagnosed cumulative carbon emissions shown in Fig. 1a.